DOI: 10.13009/EUCASS2023-895
Aerospace Europe Conference 2023 – 10TH EUCASS – 9TH CEAS

Airfoil aerodynamic optimization for Mars exploration aircraft.

Andrea Aprovitola[⋆], *Luigi Iuspa*[⋆], *Giuseppe Pezzella*[⋆†], *Antonio Viviani* [⋆]
[⋆]*University of Campania "Luigi Vanvitelli", Engineering Department*
Via Roma 29, I-81031 Aversa (CE), Italy
andrea.aprovitola@unicampania.it · luigi.iuspa@unicampania.it ·
giuseppe.pezzella@unicampania.it · antonio.viviani@unicampania.it
Corrresponding Author [†]Giuseppe Pezzella

Abstract

The red planet has always attracted attention of space scientists for research exploration activities. Currently, researchers are particularly interested in ground surface observation through high resolution images. Apart from the recently involvement of the Mars helicopter Ingenuity, to date, rovers and orbiters represent the principal way to carry out Martian surface exploration. Rovers can be used for very accurate explorations. However, they can operate only over limited areas of the planet, because of their relatively slow and rather difficult movement on surface. On the other hand, orbiters are capable of long-range explorations and cover larger areas, but with low image resolutions. Therefore, the right compromise seems to perform surface exploration by exploiting fixed-wing drones. Mars exploration through aerial drone has been an active area of research for several decades, but Martian low-density atmosphere strongly affect the aerodynamic design of the explorations aircraft. In this framework, the present paper deals with an optimization procedure able to design airfoil for fixed wing aircraft with enhanced aerodynamic performance despite the low Reynold flow conditions. To provide understanding of different Low-Reynolds design two separate airfoil parameterizations are developed and coupled to the Xfoil solver to feed the optimization procedure. A genetic algorithm is adopted to generate the optimal airfoil shape, considering the maximum efficiency as objective of optimization. Finally, the validation of the optimized airfoil is addressed by performing several computational fluid dynamics simulations in flow similarity conditions aimed at defining the airfoil aerodynamic performance.

1. Introduction

Martian exploration has always attracted attention of space scientists, especially for in ground surface observation through high resolution images.[1–3] Recently, a great achievement was obtained with the Ingenuity helicopter drone, which helped rovers and orbiters in the exploration activities of the red planet.[4–6] Rovers, such as NASA Curiosity and Perseverance allow scanning only limited area of the surface to explore, even though with high resolution images. On the other hand, orbiters are capable of long-range explorations and covers larger areas, but with low image resolutions (approximately 0.3 m/pixel) if compared to 0.1 m/pixel required for in depth observation.[7] Therefore, flying drones allow bridging the gap between local and limited aerial observation .[8–10] In particular, fixed wing aircraft are expected to fly-over on as large as possible area .[7,10] However, flying on Mars presents numerous challenges related to Aerodynamics, provided that the lower density of the atmosphere and the expected short chord length of exploration aircraft.[11,12] Therefore, cruise flight take place at rather low-Reynolds flow conditions (*e.g.*, $Re \cong 10^3 - 10^4$) and, in order to provide adequate aerodynamic lift, a high flight speed must be operated.[13] As a consequence, the onset of a fully laminar Boundary Layer (BL) on the airfoil up to the point of separation is observed [14–16] and airfoil compressibility issues are also present at lower speeds with respect to Earth .[14] In this framework, the aerodynamic performance of the exploration aircraft is dramatically affected. For instance, aerodynamic performance strongly depends on the region and extent of the BL, and on its type of separation (i.e., laminar or turbulent).[14,15]

Generally speaking, for $Re > 5 \times 10^5$, flow under the adverse pressure gradient separates and reattaches with a downstream development of a turbulent boundary layer. In this case, the dynamic pressure of separated

Copyright © 2023 by First Author. Posted on line by the EUCASS association with permission.

DOI: 10.13009/EUCASS2023-895

shear layer is high enough to drag fluid from surroundings and induce flow reattachment,[14,17]
The re-attached flow creates a Laminar Separation Bubble (LSB) inside which viscosity effects become further dominant. However, it is at very low-Reynolds (as for Martian flight) that, aerodynamic behaviour becomes non-linear. In the very low-Reynolds number regime (e.g., $Re_\infty < 5 \times 10^4$), flow separation occurs without preliminary transition to turbulent regime. The separated shear layer has not sufficient energy from the surrounding flow to reattach. Therefore, at such Reynolds number, a sub-critical flow up to the pressure recovery point is expected, and laminar flow separation is encountered.[18]
At low Reynolds number the turbulence intensity has a strong influence on flow development over the airfoil, and has to be taken into account. Specifically, several authors found a direct correlation between the increase of turbulent intensity and the delay of separation process. Therefore, at low-Reynolds, and the way it triggers the development of flow instabilities has a direct influence on aerodynamic coefficients. Increase in turbulence intensity on symmetrical NACA airfoil results in an increase in the maximum value of C_l. Below the critical value, an increase in turbulence intensity delayed stall. Winslow et al.[18] showed that the aerodynamic characteristics of a thin plate and cambered plates are better than those of the traditional airfoil at Reynolds numbers lower than 10^5.
Furthermore, formation of LSB induces flow unsteadiness and creates an apparent reduction of airfoil camber, with a consequent negative effect over the lift coefficient.[14,18] When a LSB is subjected to variation of the Angle of Attack (AoA), different characteristic length-scales (long and short bubbles) are experienced. First, with flow attachment long bubbles are formed, and with the increasing of the AoA bubbles move toward leading edge and evolve in short scale bubbles.
At these low-Reynolds conditions, airfoil design is dictated by the the necessity to realise smooth flow development on the pressure side to delay laminar separation and to increase the camber to counteract adverse pressure gradient generated by the LSB. As result of this unsteady behaviour, different type of aerodynamic issues are encountered. The LSB is responsible for a non-linear trend of the lift coefficient ,[19,20] and also of a sudden increase of pressure drag caused by laminar separation.
Consequently, aerodynamic coefficients change very rapidly with the onset of flow separation; airfoils designed, and optimized for high-Reynolds numbers flow on Earth shows a decrease of aerodynamic performances in Mars atmosphere.

In this framework, the paper focuses attention on a design procedure able to obtain an airfoil optimized for flying at low Reynolds number conditions, typical of cruise flight in Martian atmosphere. The current procedure integrates and compares two separate in-house developed models. The first one relies on a parametrization which exploits a Free Form Deformation (FFD) method, available in the open-source module *PyGem*, coupled with a specific set of parametric relations. The model is able to synchronise the vertical displacement of several control points of the airfoil in the two dimensional lattice, in order to assure reasonable airfoil shapes. The other method, denoted as synthetic model, makes use of a very limited number of high-sensitivity design parameters to generate from scratch two dimensional airfoil shapes. Both parameterization models support an optimization procedure performed via genetic algorithms and use the Xfoil tool to perform a rapid aerodynamic analysis inside the optimization cycle.
Finally, aerodynamic performance of the optimal candidates is compared also with CFD at the selected Reynolds number and also with available experimental and literature data where available. The effect of a fully turbulent and transitional model is also taken into account in the CFD simulations.

2. Low Reynolds Airfoil Aerodynamics

According to Table 1, several studies have been conducted to design airfoils or small propellers able to fly at low-Reynolds-numbers conditions, close to those experienced in Martian flight. Many of researches deal with airfoil optimization procedures, where body parameterizations are used in chain with CFD or potential-based method, coupled with genetic algorithms. Other works focuses on accurate CFD computations for various range of Re and M numbers condition. Large effort was spent on the modification of specific geometric features of the airfoil to improve its aerodynamic performances.
Sharp leading edge airfoils, with flat leeside coupled to concave windside and reduced thickness, are generally assumed as starting point to feed trade-off studies carried out with optimization procedure[18,21] Oyama et al.[13] proposed an airfoil design procedure based on a B-spline parameterization, for Mars exploration aircraft at $Re_\infty = 10^5$ and $M_\infty = 0.47$. A CFD RANS computation was coupled to a genetic algorithm, and optimal shapes were found by maximizing aerodynamic efficiency at cruise condition. Results evidenced that thin airfoils with strong camber can be used to recover lift contribution.
Jung et al.[12] formulated a multi-objective optimization procedure for an airfoil. The simulations were

DOI: 10.13009/EUCASS2023-895

Authors	Airfoil	Methodology	Reynolds	Mach	α
Oyama et al.	Mars Explorer	Optimization CFD	1.0×10^5 =	0.4 0.6	C_l 0.9
Winslow et al.	NACA0009	RANS - SA	5.0×10^4	0.1	$(6°; 8°)$
	NACA0012	=	$3.0{\times}10^5$ $1.3{\times}10^6$	= =	= =
Konig et al.	Flat plate	RANS - γRe_θ-SA	2.0×10^3	0.1	$[1°, 6°]$
	Camb. plate	=	$1.0{\times}10^4$	0.4	=
Park et al.	Propeller	Optimization CFD	1.2×10^4	0.7	$[-5°, 5°]$
Nonomura et al.	NACA 0002	laminar/iLES	2.0×10^3	0.2	$(3°; 6°; 9°)$
	NACA 0012	=	$1.0{\times}10^4$	=	=
Morgado et al.	E387	RANS - kω	2.0×10^5	n.a.	$[-1°, 15°]$
	S1223	=	$4.6{\times}10^5$	=	=
Jung et al.	Airfoil aircraft	Optimization CFD	1.5×10^5	0.6	$C_l = 0.8$
Sasaki et al.	Mars Explorer	Optimization CFD	2.3×10^4	0.2	$\alpha = 6°$

Table 1: Airfoil design procedure.

performed at $Re_\infty = 1.5 \times 10^5$ and $M_\infty = 0.65$. Optimization was performed using MOGA algorithm with Kriging model, using RANS $\gamma - Re_\theta$ model, to predict the transition point. NURBS and PARSEC parameterization were used for airfoil modelling. Optimization run for C_d and $|dC_m/d\alpha|$ minimization at fixed C_l, were strongly dependent on transition point. Optimizations performed with NURBS-based model highlighted the lowest drag coefficient.

An accurate computational assessment on various airfoils, i.e. NACA 0009, NACA 0012 airfoil, Clark-Y, flat plate airfoils, and thin cambered plates, was performed by Winslow et al.[18] Flows prediction at Reynolds numbers between 10^4 and 10^5 were conducted using a RANS flow solver with Spalart and Almarass turbulence modeling. Decreases of Reynolds number evidenced an increase in drag, due to flow separation and failure to reattach. A large decrease in lift was also observed evidencing a nonlinear behaviour below $Re_\infty = 10^5$ Effect of thickness-to-chord reduction improved the non-linearities.[18]

Numerical simulations at low-Reynolds number conditions were performed by[20] et al. where flowfield around 0012 and 0002 NACA airfoils in at $Re_\infty = 23 \times 10^3$ were studied with implicit LES. They found a different behaviour of the two airfoils with the AoA On NACA 0002 the separation occurs at leading edge and a long bubble is created by increasing AoA. While on NACA 0012 the separation point moves toward the leading edge by creating a short bubble. Sasaki et al. proposed an airfoil optimization based on a multi-objective genetic algorithm coupled with two-dimensional CFD laminar calculations. Results obtained for maximum lift and minimum drag optimization evidenced three airfoils categories, on Pareto front which shares in common a large upper surface curvature with strong curvature at the lower surface.

3. Airfoil Optimization Procedure

The general flowchart of the design procedure is shown in Fig.1. The procedure, developed in ANSYS© Parametric Design Language (APDL), is based on the following steps: i) airfoil parameterization: ii) aerodynamic computation; iii) optimization algorithm.

The Eppler 387 (E387) is selected as a baseline airfoil for the computation. This allow restricting the search to some geometric features, as mean camber line, thickness, and curvature, specific of laminar airfoils that have been shown to perform well at low Reynolds number.

The design process starts with the block A, where the airfoil geometry is provided, and continues in block B, where the design variable and their ranges of variations are assigned. Hence, in the block C two separate airfoil parameterizations are available, namely FFD-based parameterization (see block C/a) and synthetic airfoil parameterization (see block C/b), which are detailed in the following sections. Airfoil aerodynamics is addressed in block D by using the open-source code Xfoil and used to formulate objective function.

Finally, in Block D the optimization is performed and the airfoil design parameters are updated accordingly.

3.1 FFD-based Airfoil parameterization.

The FFD method is used to manipulate complex three-dimensional shape.[22,23] It uses a set of Control Points (CP) to define a lattice structure surrounding the initial body shape (see Figure 2). The lattice is chosen as

DOI: 10.13009/EUCASS2023-895

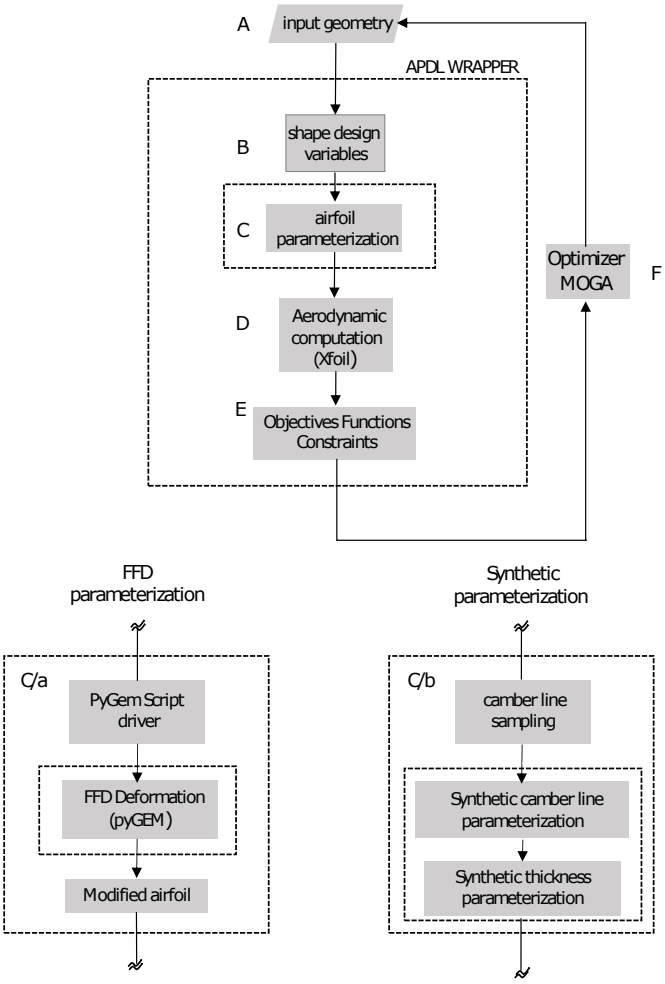

Figure 1: Flowchart of design procedure.

a rectangle for the deformation of two-dimensional bodies or a brick for the deformation of three-dimensional ones. As shown in the lower part of the Figure 2, the lattice can be then deformed by varying the coordinates of CP, managed with a set of parametric relations which express suitable mutual relocation of lattice points.

3.2 Synthetic Airfoil Parametrization

Starting from an appropriate reference airfoil, the synthetic parametrization method derives a high-sensitivity, 7-parameter synthetic airfoil geometry. The shape of E387 airfoil is used as a prototype.
The procedure involves a preliminary one-off stage of inverse geometrical analysis to derive camber line and thickness law, both approximated with a 3-point cubic spline and appropriate conditions on slope values at the ends. The purpose of this procedure is essentially to obtain suitable reference values of synthetic parameters useful as starting point in the exploration of the search space. The sequence of operations required can be summarized in the following steps:

1. from the discrete set of points representing the reference airfoil, natural splines U and L, representative of the upper and lower side respectively, are generated;

2. for an assigned parametric value u (normalized curvilinear abscissa) of U, the corresponding point $\mathbf{p}$

DOI: 10.13009/EUCASS2023-895

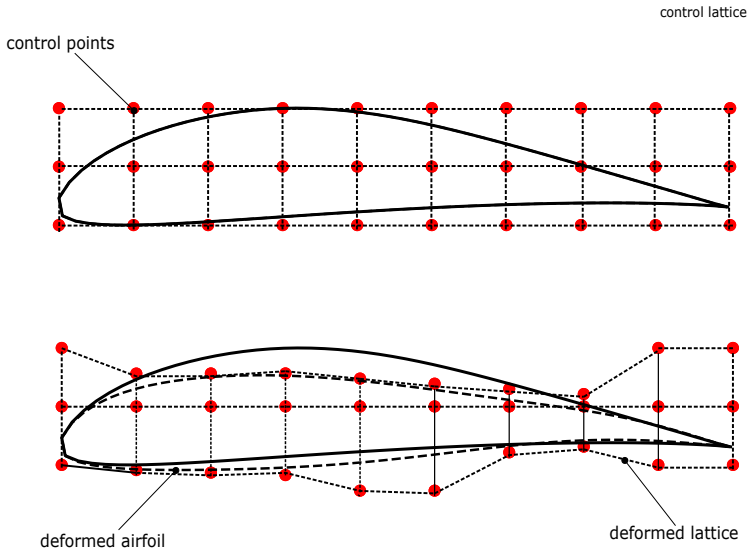

Figure 2: Pictorial representation of Control lattice (top) and deformed airfoil (down).

belonging to U and the segment N normal to U in $\mathbf{p}$, ending in $\mathbf{s}$ over L are generated;

3. an iterative procedure (e.g., halving, simple scan) driven by the parametric value n, $(0 \leq n \leq 1)$ of N selected in an interval of appropriate width bracketing the midpoint, is processed.

The parameter vector that generalizes the shape of the profile can at this point be defined with respect to the following parameters:

$Xpos$ Position in tenths of chord of the point of maximum camber;

$Ypos$ Value in hundredths of chord of the maximum camber;

$CSlop$ Slope of the average line @$\boldsymbol{TE}$;

$Maxx$ Position in tenths of chord of the point of maximum thickness;

$Maxy$ Value of maximum x10 thickness in hundredths of chord;

$Tslop1$ Slope of the x10 thickness @$\boldsymbol{LE}$;

$Tslop2$ Slope of the x10 thickness @$\boldsymbol{TE}$;

The synthetic, approximated representation of the reference Eppler387 derived by applying the above-described reverse geometry stage is represented by the parametric values shown in Table2, while in Fig.3, a graphical representation of the above-described parameters is given. The regular procedure for constructing

dV	Name	min.
$Xpos$	0.391161614	ad
$Ypos$	0.037921572	ad
$Cslop$	5.825666	ad
$Maxx$	0.326551242	ad
$Maxy$	0.0453205448	ad
$Tslop1$	95.021221	deg
$Tslop2$	24.391232	deg

Table 2: Reference values for the synthetic approximated representation of the Eppler387 airfoil.

a generic parametric airfoil can then be obtained by conceptually reversing the points described for the one-off preliminary stage.

DOI: 10.13009/EUCASS2023-895

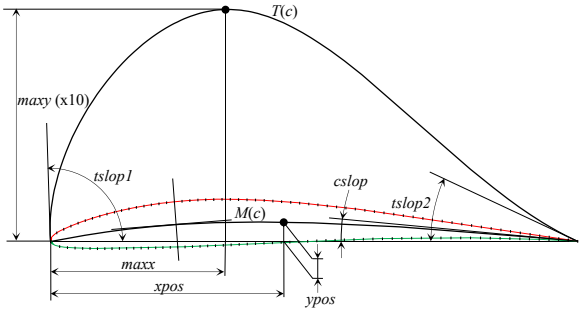

Figure 3: Centerline and thickness parametric controls.

3.3 Aerodynamic analysis

Aerodynamic computations are carried out with *Xfoil*, a vorticity-based solver, suitable for subsonic flows.[24] The tool is also able to perform viscous computations, being provided with an integral boundary layer method, and results reliability at low-Reynolds number conditions was proven in previous research works.[11,15] Anyway, several flowfield simulations have been carried out within the present research effort to feed *CFD-Xfoil* result comparisons in order to address results accuracy. Code robustness makes *Xfoil* specifically suitable in optimization problems, where a high number of evaluations are required to assure convergence of the procedure. *Xfoil* simulations are conducted by leaving the code to determine position of transition point to a fully turbulent regime with the approximate e^N method. The default value $N = 9$ is adopted to compute initial turbulence level.[15,24] A number of 250 panel is assumed to provide a trade-off between accuracy of computation and computational cost. A step size increment of 0.5° is given to provide the current computed solution starting guess of new AoA.

4. Reliability of Xfoil computation at low Reynolds

Airfoil Aerodynamics at Low-Reynolds conditions is very sensitive to prediction of laminar separation, transition, and eventually to turbulent reattachment.[18] *Xfoil* outcomes are validated against CFD results provided by simulations with the commercial ANSYS-FLUENT^{TM} software,[25] the open-source toolkit SU2,[26] and experimental data coming from several wind tunnel test campaigns.[5] This bench-marking phase was carried out considering the aerodynamics of the E387 airfoil at two Reynolds numbers, namely $Re_\infty = 2 \times 10^5$ and $Re_\infty = 6 \times 10^4$. At the greater Reynolds number, laminar separation followed by turbulent reattachment is very likely to happen ,[14,27] while at $Re_\infty = 6 \times 10^4$ the relative importance of laminar separation phenomena on the rapid increase with AoA of aerodynamic drag becomes significant,[5].[28]

4.1 CFD computations of E387 at $Re_\infty = 2 \times 10^5$

The aerodynamic analysis of E387 at $Re_\infty = 2 \times 10^5$ was accomplished by means of steady state RANS simulations in fully turbulent regime with Shear Stress Transport k $-\omega$ turbulence model with low Reynolds correction.[29] A multiblock structured grid with 142900 points and a fully resolved boundary layer was generated assuring that the first cell at wall corresponds to a $y^+ \leq 1$. The inlet and outlet boundaries were placed 50 and 100 body lengths away from the airfoil, respectively. Flow speed at the domain inlet is prescribed by adopting farfield boundary conditions corresponding to $H_\infty = 8km$ and $M_\infty = 0.0195$. Wall boundary conditions are adopted on both airfoil leeside and windside. The density-based solver available in ANSYS-FLUENT is adopted in the current computation. Spatial discretization of inviscid terms is performed using second-order upwind scheme, while gradients at cell centers are obtained by using the Least-Squares Cell-Based (LSCB) method.[25]
In Figure 4A-D the comparisons between the current CFD computation, CFD computation of Morgado et al.,[15] and experimental data of McGhee et al.,[29] are shown. As one can see, Figures 4 C,D show that Xfoil predicts rather well the aerodynamic coefficients in the whole α range. Underestimation of drag coefficients with respect CFD computation is observed for $\alpha \in [7°, 8°]$. At $\alpha > 8°$ the non-linearity of lift coefficient is also predicted by Xfoil as it can be observed in Figure 4C,D.

DOI: 10.13009/EUCASS2023-895

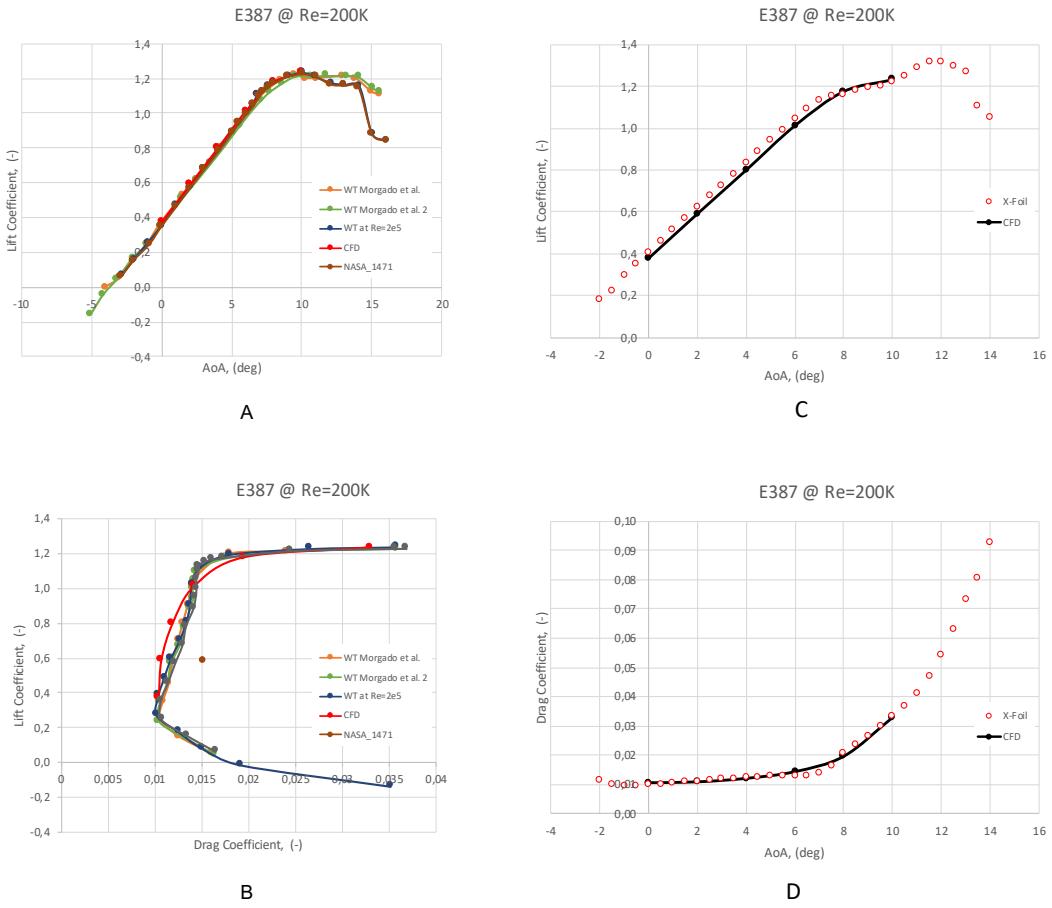

Figure 4: CFD computation for E387 airfoil versus experimental wind tunnel data (A); CFD computation for E387 airfoil versus Xfoil computation (B).[15,29]

4.2 CFD computation of E387 at $Re_\infty = 6 \times 10^4$

A further validation of Xfoil at low-Reynolds number conditions is performed using again the E387 airfoil. CFD simulations for freestream Reynolds and Mach numbers equal to $Re_\infty = 6 \times 10^4$ and $M_\infty = 0.05$, respectively, and the experimental data provided in Ref.[5] are considered as reference data with which to compare the results of Xfoil. The freestream conditions relates to a total pressure and to a turbulent intensity level (in the pressurized wind tunnel chamber) equal to: $p_t = 34473$ Pa and $Tu = 0.16\%$, respectively . Steady RANS simulations are performed with the SU2 compressible solver. The second order Low-Dissipation Low-Mach (L2ROE) scheme is used for inviscid flux discretization, while the second order accurate weighted least square scheme is adopted for diffusive discretization. Farfield boundary conditions are adopted at the domain inlet and outlet, while wall adiabatic boundary condition is adopted on the airfoil surface. The transition model used in present computations is the Langtry-Menter (LM) four equations Transitional SST model also known as $\gamma-$ Re$_\theta-$SST model.[30] It is based on the k-ω SST model coupled with the intermittency function γ which trigger the transition. The model equation of the intermittency function is coupled with the SST turbulence model to onset the production of turbulent kinetic energy. The model is provided also with an equation for the momentum-thickness Re number to describe non-local influences of turbulence intensity and pressure gradients. The current version of LM model implemented in SU2 by Rausa et al.[31] allows to compensate the low-turbulence intensity level in the separated shear layer regions. The intermittency function value is artificially modulated to trigger flow reattachment by assuming value $\gamma > 1$. Steady RANS simulations are performed at $\alpha = 0°, 2°, 4°, 5°, 6°, 8°$ to verify prediction of laminar separation and the laminar separation bubble position. Result comparisons in terms of pressure distributions among Xfoil, SU2, and experimental data is shown in Fig.5. As shown, both numerical predictions compare rather well

DOI: 10.13009/EUCASS2023-895

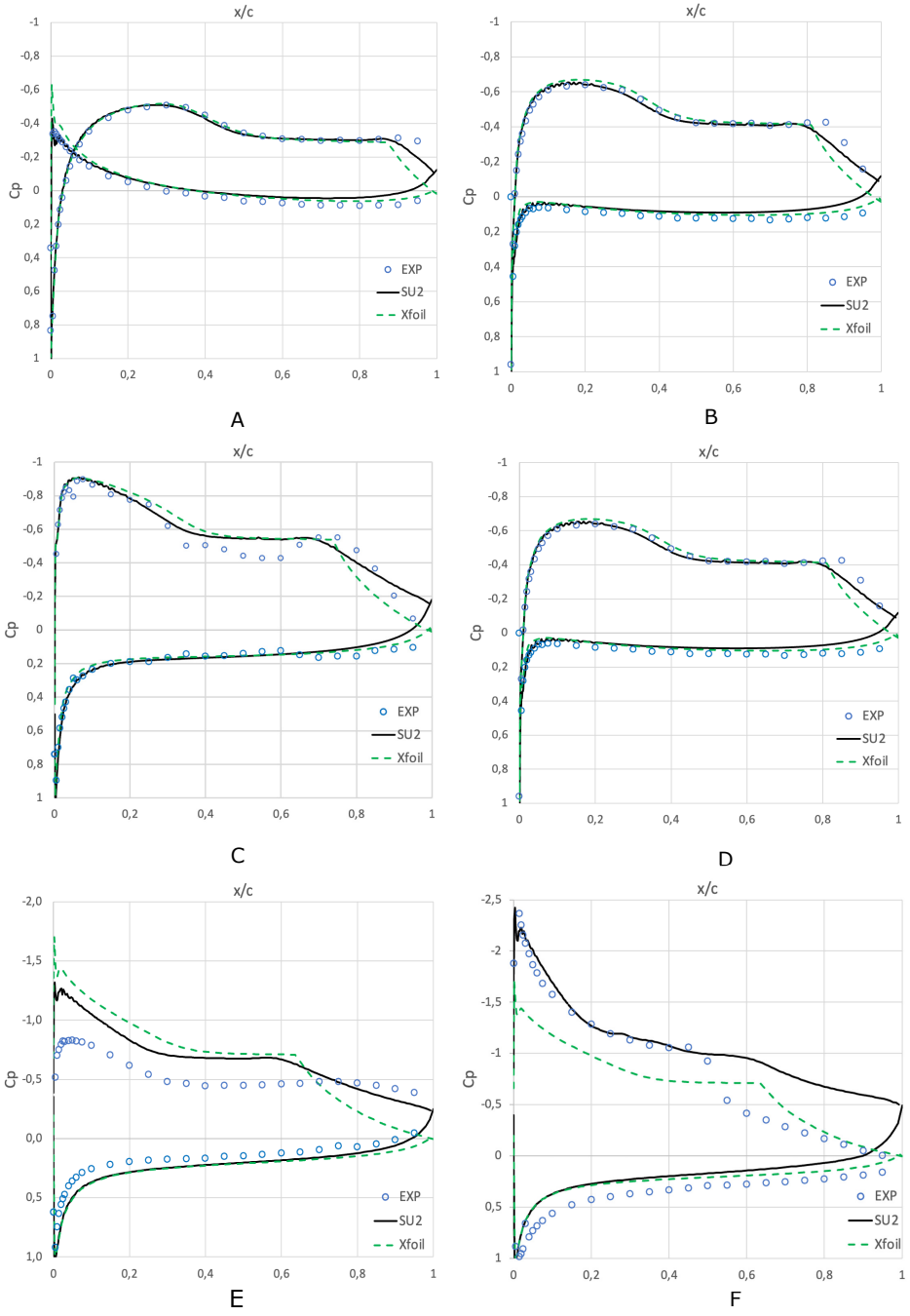

Figure 5: A-F Pressure coefficients at simulated AoA: (A) $\alpha = 0°$; (B) $\alpha = 2°$; (C) $\alpha = 4°$; (D) $\alpha = 5°$; (E) $\alpha = 6°$; (F) $\alpha = 8°$.[5]

with experimental data.[5] Additionally, comparisons confirm that both laminar separation and turbulent reattachment points (evidenced by the plateau in the pressure coefficient profile) are well predicted by the Xfoil and CFD simulations to up $\alpha = 5°$. At $\alpha = 6°$ the CFD data underestimate the pressure expansion peak. Recall that, this behaviour has also been observed in Ref.,[18] and it is due to the inability of the simulation to predict aerodynamic non-linearities which occurs at low-Reynolds.

The nonlinear behaviour of aerodynamic coefficient is associated to the migration phenomena of the laminar separation bubble, on the suction-side of the airfoil, from T.E. toward L.E. Finally, for $\alpha > 8°$ a substantial inaccuracy of CFD simulation to predict aerodynamic coefficients, is observed. Specifically, for this AoA, low turbulent kinetic energy level has been detected in the region of the separated shear layer. Therefore, a consequent reduction of reattached flow region is experienced which causes a lower expansion peak.[31]

DOI: 10.13009/EUCASS2023-895

Function name	Admissible range
Aerodynamic Efficiency OBJ	Max in $\alpha \in [0°, 7°]$

Table 3: Objective for the optimization problem.

5. Airfoil Optimization

The FFD-based parameterization and the Synthetic Parametrized Representation are applied in two single-objective optimizations denoted in the following as **Opt_I** and **Opt_II**, respectively, according to the design procedure shown in Section 3. The optimization assumes to maximise airfoil aerodynamic efficiency in the range of AoA $[0°, 7°]$. The selected range of α refers to a cruising flight condition on Mars (e.g., $[0°, 4°]$), with further increment of α to provide off-cruise flight conditions. The general formulation of the optimization problem is described as follows:

$$\begin{cases} max f(\mathbf{x}); & \mathbf{x} = (x_1, \ldots, x_n) \\ \underline{x}_i \leq x_i \leq \overline{x}_i & i = 1, n \\ \underline{g}_j \leq g_j(\mathbf{x}) \leq \overline{g_j} \end{cases} \tag{1}$$

being $\mathbf{x}$ the vector of design variables and $\underline{g_j}$ and $\overline{g_j}$ the $j-th$ constraints. The objective function, design variables, and bounding limits for both parameterizations are summarized in Table 3, Table 4 and Table 5 for both optimization procedures.

dV	Symbol	Min. value	Max. value	Unit
P_{p2}	Δy_{p2}	-0,5	0.5	ad
P_{p3}	Δy_{p3}	0.0	0.6	ad
P_{p4}	Δy_{p4}	0.0	0.7	ad
P_{p5}	Δy_{p5}	0.0	0.2	ad
P_{p6}	Δy_{p6}	-0,1	0.1	ad
P_{p7}	Δy_{p7}	-0,1	0.1	ad
P_{p8}	Δy_{p8}	-0,1	0.1	ad
P_{p9}	Δy_{p9}	-0,1	0.1	ad
P_{m2}	Δy_{p2}	-0,5	0.5	ad
P_{m3}	Δy_{p3}	0.0	0.6	ad
P_{m4}	Δy_{p4}	0.0	0.7	ad
P_{m5}	Δy_{p5}	0.0	0.2	ad
P_{m6}	Δy_{p6}	-0,1	0.1	ad
P_{m7}	Δy_{p7}	-0,1	0.1	ad
P_{m8}	Δy_{p8}	-0,1	0.1	ad
P_{m9}	Δy_{p9}	-0,1	0.1	ad

Table 4: Side constraints for design variables (FFD parameterization).

First, shape profile optimizations at $Re_\infty = 2 \times 10^5$ are performed. Optimal candidate performance is

dV	Symbol	Min. value	Max. value	Unit
XPOS	X_{pos}	0,2	0.5	ad
YPOS	Y_{pos}	0,02	0.06	ad
CSLOP	C_{slop}	0	23	ad
CSLOP	C_{slop}	0	23	ad
MAXX	MAX_X	0.22	0.55	ad
MAXY	MAX_Y	0.25	0.55	ad
TSLOP1	$TSLOP_1$	92	105	ad
TSLOP2	$TSLOP_2$	10	35	ad

Table 5: Side constraints for design variables (Synthetic parameterized representation).

further compared with CFD and with experimental wind tunnel data.[15] Therefore, it represents a preliminary benchmark of the optimization procedure.
A further optimization stage at very low-Reynolds number (i.e. $Re_\infty = 34 \times 10^3$) has been also performed to determine the optimal airfoil in true Mars atmosphere flight conditions.

DOI: 10.13009/EUCASS2023-895

5.1 Airfoil Optimizations at $Re_\infty = 2 \times 10^5$

The first test-case (Opt_I) is performed using the floating-point version of MOGA Genetic Algorithm (GA) implemented in ANSYSÂ® Workbench.[25] The GA is initialized assuming an initial population of 200 individuals for an adequate initial sampling of the search space. A populations of 100 individuals is then defined for the iterative evolutionary process to assure a robust convergence of the algorithm. Finally, a convergence criterion of 2% on the stability of the population has been adopted.[25]
For Opt_II a different optimization algorithm has been chosen, i.e. the zero-order Powell Method (SUMT) available in ANSYS-Workbench. The choice of a more efficient but less robust deterministic optimization algorithm is justified by a much limited search space (just seven design parameters), derived by the synthetic parameterization, and also because of, at this preliminary stage, only a preliminary validation of the procedure is concerned. As far as results are concerned, Fig6A-B show the convergence history of objective

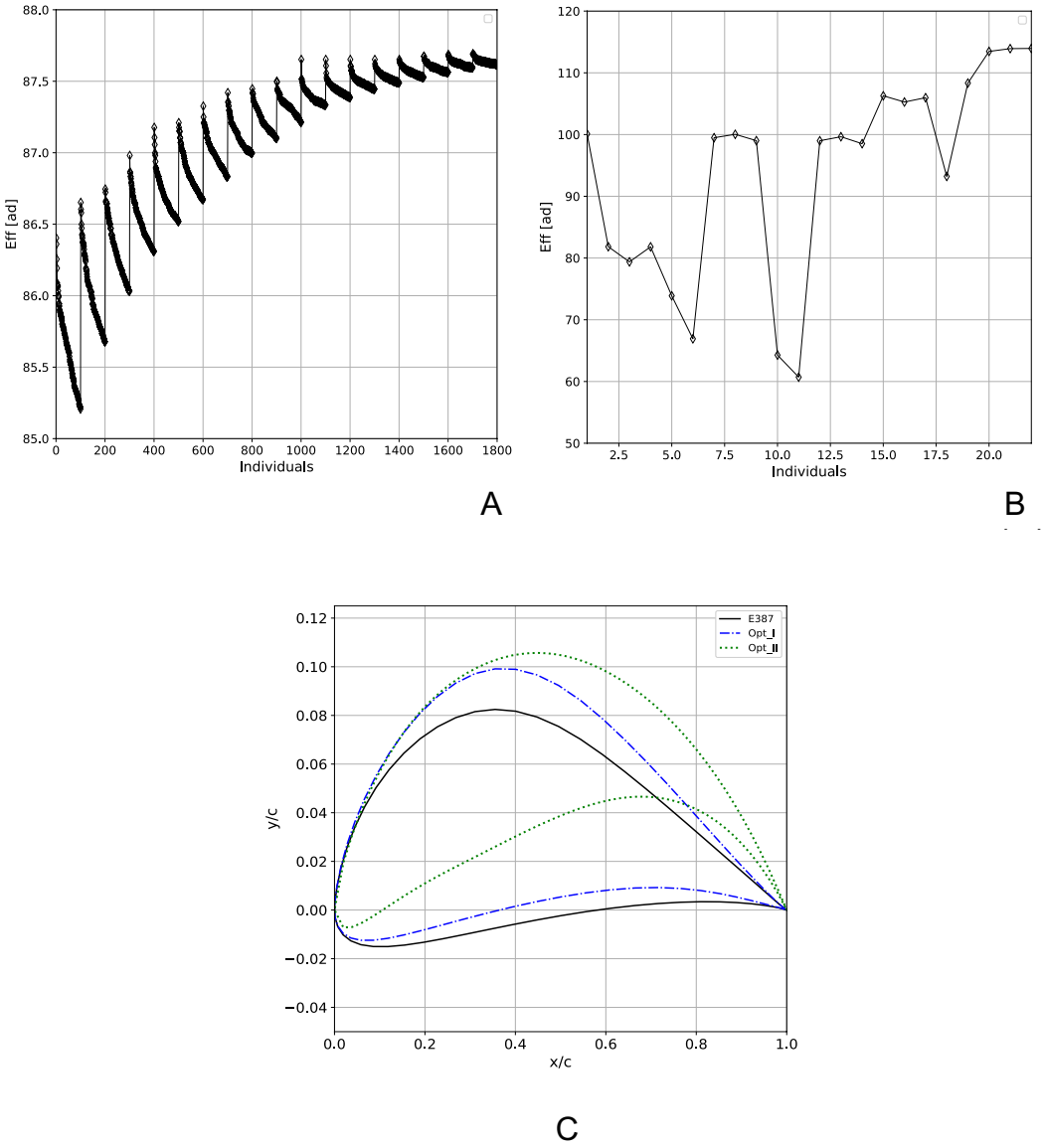

Figure 6: Convergence history of objective function: A-Opt_I, B-Opt_II, C-Optimal shapes.

functions for the two optimisations, respectively. As one can see, Opt_I has reached convergence after 23 generation, which correspond to 1873 evaluations of the objective function, while Opt_II has reached convergence after 22 iterations. Optimal airfoil candidates compared with the baseline E387 wing section are shown in Figure 6-C. Additionally, Table 6 summarises the airfoil geometric features and $(L/D)_{max}$ values

DOI: 10.13009/EUCASS2023-895

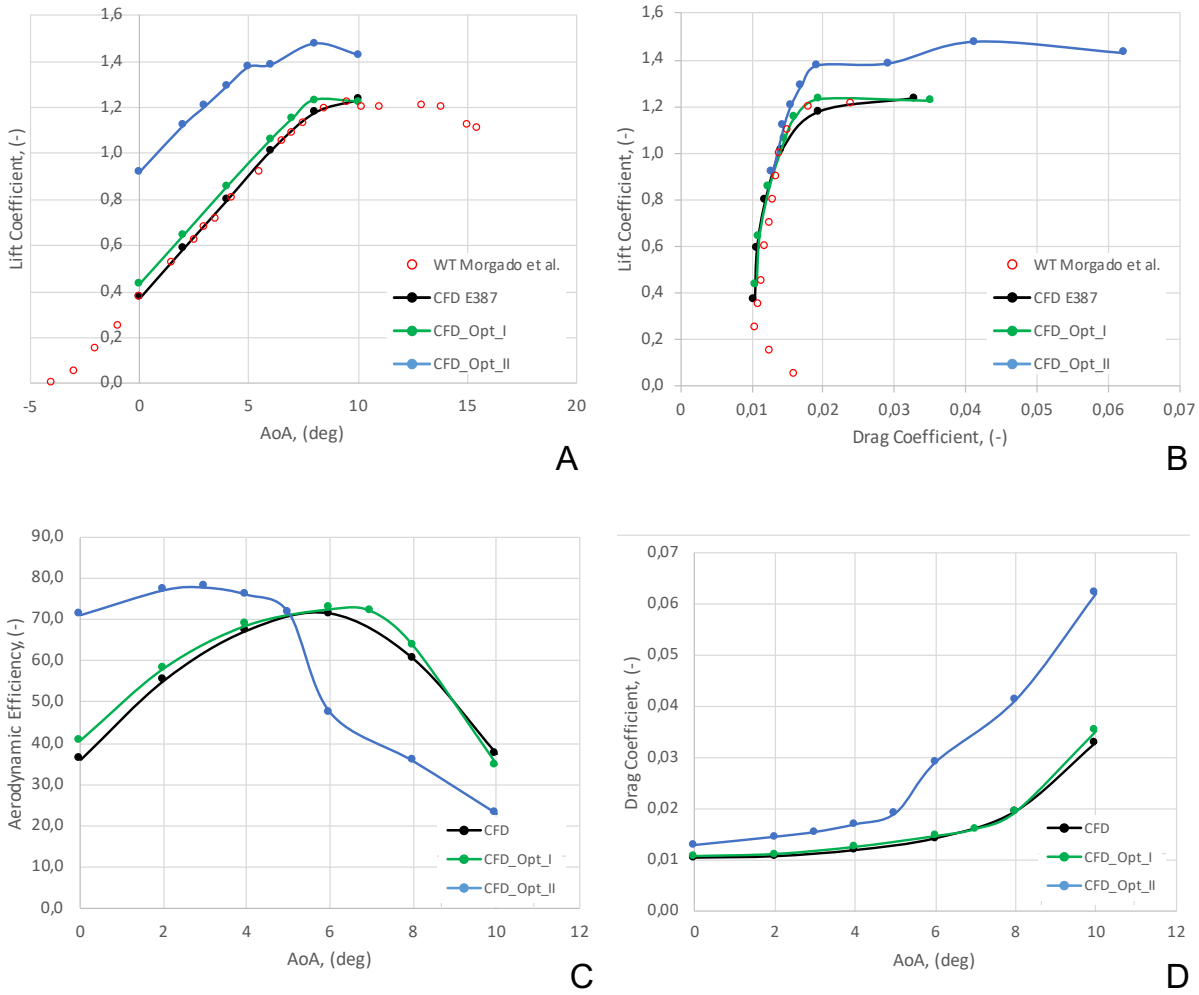

Figure 7: Aerodynamic performance comparison for optimal candidate: (A) lift coefficient; (B) drag polar; (C) Aerodynamic coefficient; (D) drag coefficient.

in the range of AoA $[0°, 7°]$.

A preliminary consideration to address is that aerodynamic performances with Xfoil appear to be over-predicted by CFD data (see Table 6) if compared to fully turbulent RANS simulations. A possible explanation to this could be related to the lack of transition model in the CFD simulation. Results of Table 6 indicates, for both optimal candidates, that improvement of $(L/D)_{max}$ can be ascribed to a more cambered airfoil compared to the baseline E387 configuration. It is worth noting that moderate increment of $(L/D)_{max}$ can be appreciated for Opt_I compared to Opt_II. For both models the increase of maximum camber appears to be positively correlated to the increase of airfoil aerodynamic efficiency.

This conclusion agrees with previous studies which evidence that occurrence of LSB on the suction side can be positively counterbalanced by increasing the camber.[14] Furthermore, the increase of maximum camber is correlated to a decrease of maximum thickness τ/c for Opt_II. This result is expected because the synthetic parameterization allows a more sensitive and direct influence on thickness distribution, compared to FFD-based parameterization. In this last case, a set of effective shapes can be obtained only within in a very limited excursion of the control points with respect to the reference positions. Furthermore, the overall displacements of the control points must be congruently synchronised along the airfoil chord. However, this implicit (shape) constraint introduced by FFD parameterization, reflects in a quite linear trend of aerodynamic coefficient as shown in Figure 7A-C.

A different trend of aerodynamic coefficients is found for Opt_II. Figure7C shows that the highest value $(L/D)_{max}$ is obtained in the range $[0°, 4°]$. Moreover, optimal candidates obtained shows a higher C_D and C_L with a marked non linearity of C_D at $\alpha > 5°$. Therefore, an higher $(L/D)_{max}$ in cruise condition reflects to a non-linearity of aerodynamic behaviour of the optimal airfoil in off-design conditions.

DOI: 10.13009/EUCASS2023-895

Airfoil	Max. Thickness	Max. Camber	Max. Eff (Xfoil)	Max. Eff (CFD)
E387	9.1 % @ 31% c	3.2% @ 44% c	84.4 @ $\alpha = 6.7°$	71.5 @ $\alpha = 6°$
Opt_I	9.3 % @ 31% c	4.4% @ 40 % c	87.6 @ $\alpha = 6.2°$	72.7 @ $\alpha = 6°$
Opt_II	7.7 % @ 31% c	7.1% @ 54 % c	113.4 @ $\alpha = 3°$	77.8 @ $\alpha = 3°$

Table 6: Optimal airfoil features comparison between CFD and Xfoil computation.

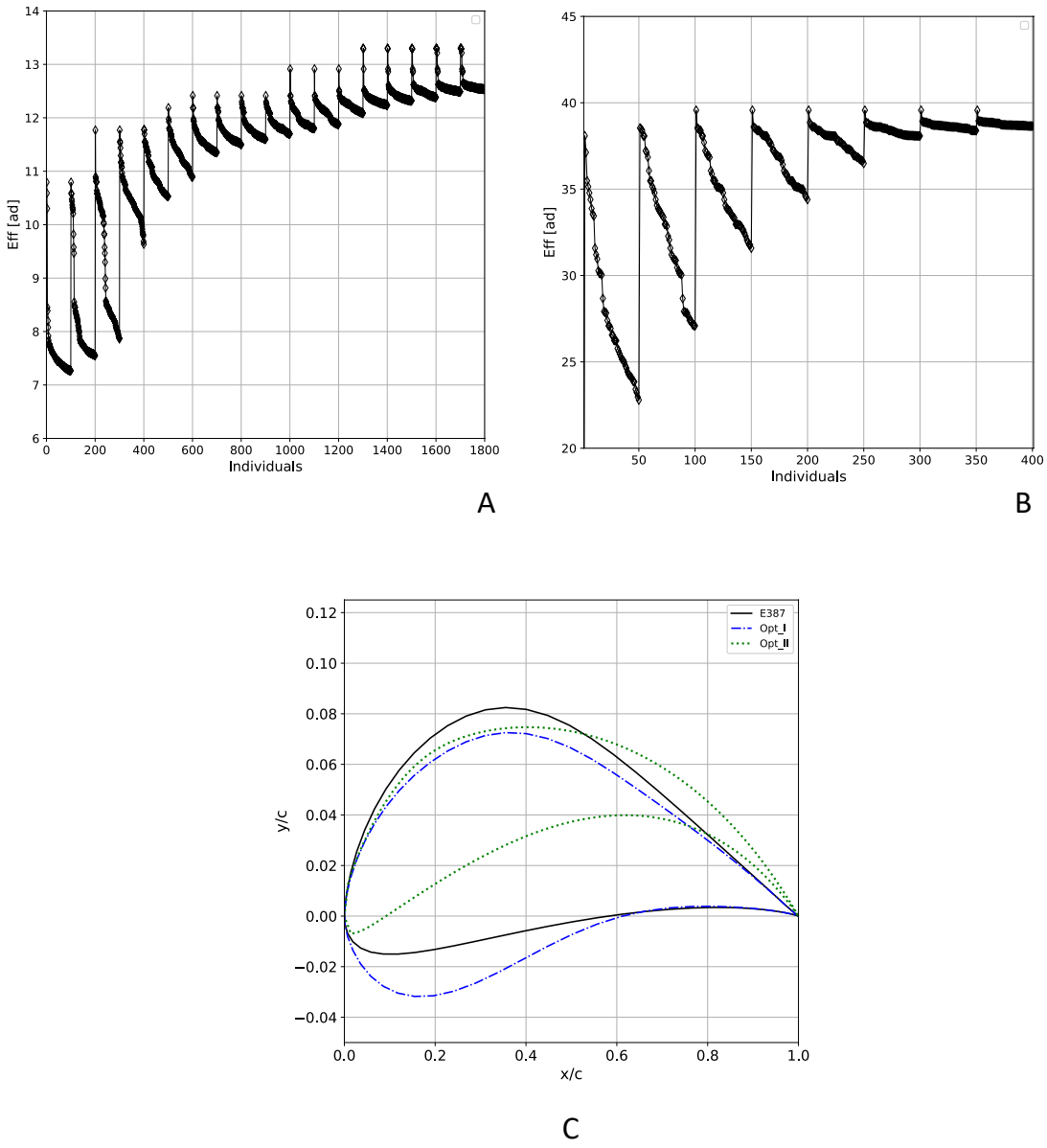

Figure 8: Convergence history of objective functions: A-Opt_I , B-Opt_II; C-Optimal airfoil shape.

5.2 Airfoil Optimizations at $Re_\infty = 34 \times 10^3$

To simulate flight conditions in Mars atmosphere, further optimizations (see Table 3) have been performed at $Re_\infty = 34 \times 10^3$ and $M_\infty = 0.05$ freestream conditions, with a turbulent intensity level equal to $Tu = 0.16\%$. At this stage the MOGA algorithm is adopted for both optimizations of Table 3, with the ranges of design variables assigned in Table 4 and Table 5 for Opt_I and Opt_II, respectively. Opt_I is initialized assuming the same initial population and number of individuals per generation adopted at $Re_\infty = 2 \times 10^5$. Convergence is obtained after 11 iterations corresponding to 1186 evaluations of the objective function.
Opt_II is initialsed with a smaller initial population equal to 100 individuals, with 50 individuals generated

DOI: 10.13009/EUCASS2023-895

at each iteration. Convergence for Opt_II is obtained after 8 generations equivalent to 400 evaluations of the objective function. In Figure 8A-C, convergence history of the objective functions for problems Opt_I and Opt_II is shown, respectively. Optimal airfoil candidates are shown in Fig.8-C and airfoil geometric features in Table 7.

Airfoil	Max. Thickness	Max. Camber	Max. Eff (Xfoil)	Max. Eff (CFD)
Opt_I	9.6 % @ 26% c	3.4% @ 44 % c	30 @ $\alpha = 7^{\circ}$	10.39 @ $\alpha = 4^{\circ}$
Opt_II	7.7 % @ 31% c	7.1% @ 54 % c	38 @ $\alpha = 6.5^{\circ}$	16.45 @ $\alpha = 4^{\circ}$

Table 7: Optimal airfoil features comparison between CFD and Xfoil computation.

As far as CFD results are concerned, in Figure 10 and Figure 9 the non dimensional pressure distribution related to CFD and Xfoil data, for Opt_I and Opt_II are shown, respectively. Pressure distribution

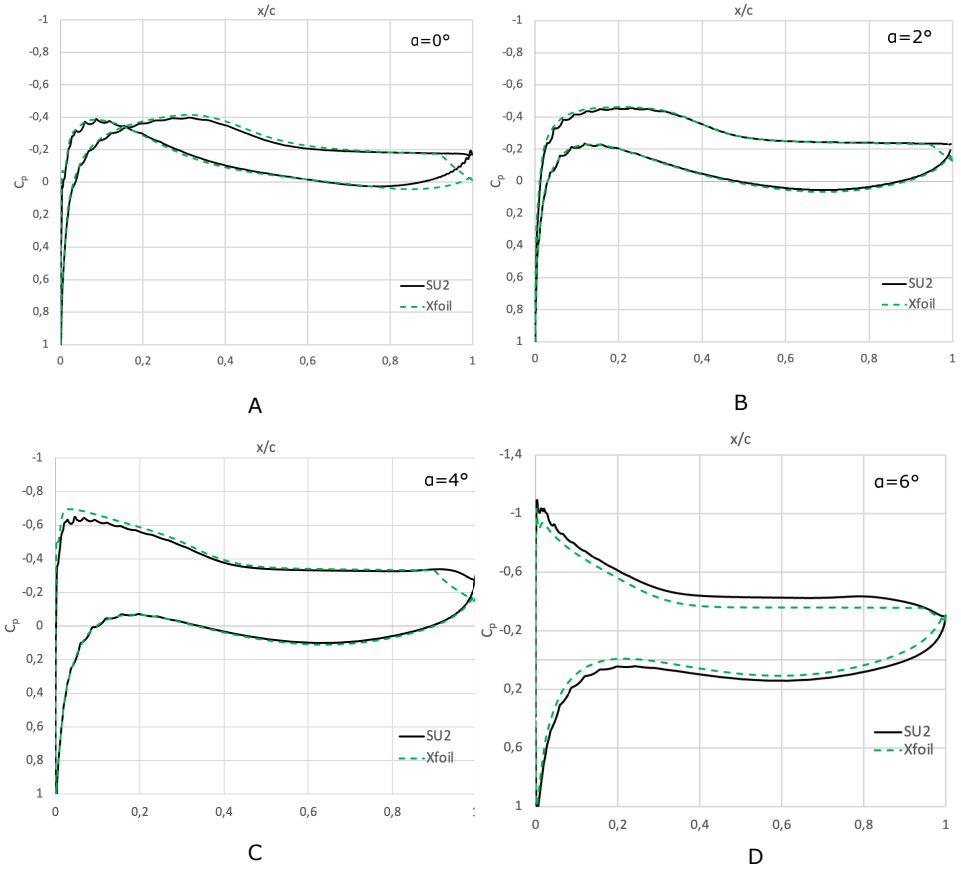

Figure 9: Opt_I: pressure coefficients at simulated AoA: (A) $\alpha = 0^{\circ}$; (B) $\alpha = 2^{\circ}$; (C) $\alpha = 4^{\circ}$; (D) $\alpha = 6^{\circ}$.

comparisons show that Xfoil results agrees fairly well with CFD ones. The good agreement obtained with CFD data confirms that Xfoil, provides reliable aerodynamic predictions to optimization algorithm. Differences between Xfoil predictions and SU2 simulations are particularly observed at $\alpha = 6^{\circ}$ for Opt_I and at $\alpha = 0^{\circ}, 2^{\circ}$ for Opt_II. As a first explanation to this differences, it can be considered that at this low Reynolds number, the approximate transition method employed in Xfoil tend to overestimate the expansion on the suction side, for high curvature airfoils.[15] This is specifically observed for optimal candidate Opt_II.
The above mentioned observation agrees with the results obtained in[18] for cambered plates, which have shown to demonstrate an increase of L/D ratio, and a non-linearity of aerodynamic coefficient, with hysteresis on lift coefficients. This behaviour can be explained with the formation and movement of a LSB. By increasing α, simulations shows the forward movement (T.E. to L.E.) of laminar-to-turbulent transition point, on the suction side. However, observation of non-dimensional pressure distribution (see Fig.10A-C), shows that flow reattachment is not observed. The above observation agrees with Xfoil prediction as shown by the good matching of pressure distributions with CFD simulation. However, due to the difference in the transition model between SU2 and Xfoil, an appreciable difference on airfoil aerodynamic efficiency is observed.

DOI: 10.13009/EUCASS2023-895

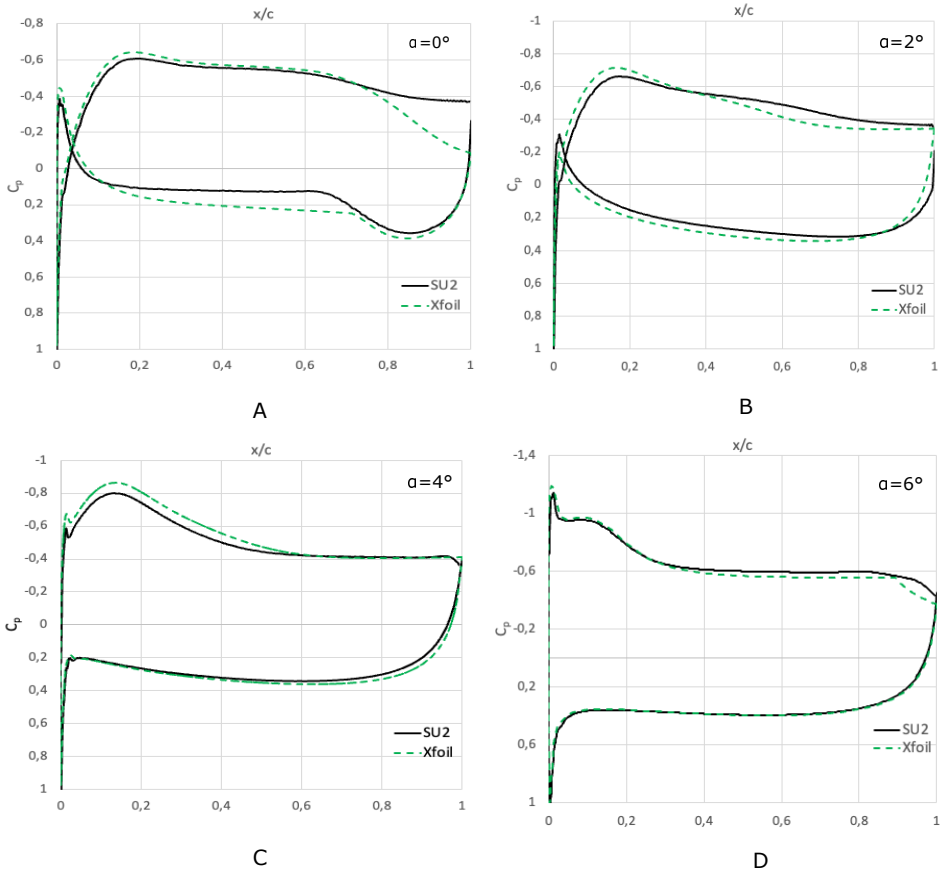

Figure 10: Opt_II: pressure coefficients at simulated AoA: (A) $\alpha = 0°$; (B) $\alpha = 2°$; (C) $\alpha = 4°$; (D) $\alpha = 6°$.

Specifically, $(L/D)_{max} = 10.39$ for Opt_I and $(L/D)_{max} = 16.45$ for Opt_II. This difference is due to the inaccuracy of drag estimation in the approximate transition e^N model in Xfoil at such low Reynolds number. Anyway, two different aerodynamic behaviours of optimal shape are associated to the maximization of L/D. Assuming the E387 airfoil as comparison, $(L/D)_{max}$ is associated to the reduction of maximum thickness for Opt_II, where the maximum thickness is equal to 7.7%; while is substantially unaffected in the Opt_I (see Figure 8 and Table 7). Additionally, the same observation can be derived for the camber value. An $(L/D)_{max} = 38$ is found in Opt_II, while $(L/D)_{max} = 30$ was found in Opt_I.
Comparison of optimized airfoil for Opt_I and Opt_II at $Re_\infty = 2 \times 10^5$ and $Re_\infty = 3.4 \times 10^4$ (see Fig. 6 and Fig.8), shows that an higher curvature of the windside at $Re = 34^3$ is obtained associated to a thickness reduction. This evidence can be explained by considering that low Reynolds determines an higher flow sensitivity to external disturbance and viscosity effect. Therefore, maximum value of L/D in cruise flight condition can be obtained by increasing the expansion on the lower side with a strong camber. This geometric feature is able to counteract the effect of early laminar separation on the suction side, where laminar flow development is expected.[13,18]
In addition, it is worth noting that at lower Reynolds optimal candidates show different shapes between developed parameterizations. Specifically, the optimal candidate found in Opt_I has a smoother suction side to prevent early laminar separation; while Opt_II airfoil favors transition and obtains $(L/D)_{max}$ by increasing curvature on the pressure side. Therefore, although for both Re optimization trends to maximize L/D by featuring a camber increase, this effect is more evident at low-Reynolds number and for synthetic airfoil parameterization.

6. Conclusions

This paper dealt with airfoil aerodynamic optimization applied to conceptual design of future fixed-wing Mars explorers. To this aim, two aeroshape parameterizations based on different modelling approach have been

DOI: 10.13009/EUCASS2023-895

developed and integrated in the framework of an optimization loop for a maximum aerodynamic efficiency objective. Optimization run performed respectively at $Re_\infty = 2 \times 10^5$ and $Re_\infty = 34 \times 10^3$ revealed that at the selected Reynolds numbers, airfoils exhibited a thinner profile compared to the common thickness distribution of a laminar airfoil. Several geometric features common to both the optimizations evidenced the effect of Reynolds number on the optimal shape. For both optimal airfoils, the thickness reduction is always associated to a camber increase to enhance the lift characteristics of the airfoil. The two shape parameterizations adopted i.e. the FFD parameterization and the synthetic shape representation, reflected the maximization of aerodynamic efficiency at cruise angle of attack with different shape but with similar geometric feature. The synthetic airfoil representation realized the maximum aerodynamic efficiency objective, with an high curvature profile on the pressure side to compensate the effect of laminar separation. The FFD-based parameterization also reflects the same design trend of the synthetic airfoil representation. However, the parameterization features the maximization of lift-to-drag with a larger thickness and low curvature radius to keep the laminar flow development.

References

[1] Engineering National Academies of Sciences and Medicine. Visions into voyages for planetary science in the decade 2013 2022: A midterm review. The National Academies Press:Washington, DC, USA, 2018.

[2] National Research Council. Vision and voyages for planetary science in the decade 2013â2022. The National Academies Press:Washington, DC, USA, 2021.

[3] N. Barlow. Mars: An introduction to its interior, surface and atmosphere. Cambridge University Press, New York, 2014.

[4] C. Duncan M. Golombek H. F. Grip W. Johnson J. Maki A. Quon R. Stern D. Zhu J. B. Barlow, T. Canham. Mars helicopter technology demonstrator. AIAA Science and Technology Forum and Exposition (AIAA SCitech), 2018.

[5] Hibbard D. Turtle E. Lorenz R. Amzajerdian F. Langelaan J. T. McGee, D. Adams. Guidance, navigation, and control for exploration of titan with the dragonfly rotorcraft lander. in 2018 AIAA Guidance, Navigation and Control conference, 2018.

[6] P.T. Tokumaru J. Balaram. Rotorcraft for mars exploration. in 11th International Planetary probe Workshop 2014, 2018.

[7] T. Schuler S. Shkarayev H. Kalita A. Bouskela, A. Kling and J. Thangavelautham. Mars exploration using sailplanes. Aerospace MDPI, 9(306), 2022.

[8] S. Chen T. Yang D. Bai D. Tang Z. Deng P. Zhao, Q. Quan. Geometry shape selection of naca airfoils for mars rotorcraft. Acta Astronautica, 157:300–309, 2009.

[9] V. J. Lappas J. L. Forshaw. Architecture and systems design of a reusable martian twin rotor tailsitter. Acta Astronautica, 80(80):166–180, 2012.

[10] C. Kuhl. Design of a mars airplane propulsion system for the aerial regional-scale environmental survey (ares) mission concept. Proceedings of the 44th AIAA/ASME/SAE/ASEE Joint Propulsion Conference Exhibit, Reston, VA, USA, 2008.

[11] S. JEONG K. Park, J. jung. Multi-objective shape optimization of airfoils for mars exploration aircraft. International journal of Aeronautical and space sciences, 2022.

[12] T. MISAKA S. JEONG J. JUNG, K. YEE. Low reynolds number airfoil design for a mars exploration airplane using a transition model. Trans. Japan Soc. Aero. Space Sci., 60(6), 2017.

[13] K. Fujii A. Oyama. A study on aifoil design for futre mars airplane. AIAA paper, 2006-1484.

[14] W. Johnson W. F. Koning, E.A. Romander. International 74th annual forum technology display, phoenix, arizona, usa. 2017.

[15] M.A.R. Silvestre J.C. Pascoa J. Morgado, R. Vizinho. Xfoil vs cdf performance predictions for high lift low reynolds number airfoils. Aerospace Science and Technology, 52, 2016.

DOI: 10.13009/EUCASS2023-895

[16] A. Oyama R. Kojima, T. Nonomura and K. Fujii. Large'eddy simulation of low'reynolds number flow over thick and thin naca airfoils. Journal of Aircraft, 50(1), 2013.

[17] Hall J. and Mohseni K. Numerical simulation of an airfoil at low reynolds number. 45th AIAA Aerospace Sciences Meetings and Exhibitions, 8-11 January 2007, 2007.

[18] B. Govindarajan J. Winslow, H. Otsuka and I. Chopra. Basic understanding of airfoil characteristics at low reynolds numbers (10^4-10^5). Journal of Aircraft, 55(3), 2018.

[19] M. Drela. Transonic low-reynolds number airfoils. J. Aircraft, 29(6), 1992.

[20] A. Oyama K. Fujii R. Kojima, T. Nonomura. Large-eddy simulation of low-reynolds nmber flow over thick and thin airfoils. Journal of Aircraft, 50(1), 2013.

[21] T. Nonomura A. Oyama T. Matsumoto G. Sasaki, T. Tatsukawa and K. Yonemoto. Multi-objective optimization of airfoil for mars exploration aircraft using genetic algorithm. Transaction JSASS Aerospace Tech. Japan, 2014.

[22] S. R. Parry T. W. Sederberg. Free-form deformation of solid geometric models. SIGGRAPH Comput. Graph. 20, pages 151–160, 1986.

[23] L. Yan T. tian Zhang Y. Shen, W. Huang. Constraint-based parameterization using ffd and multi-objective design optimization of a hypersonic vehicle. Aerospace Science and Technology, (100), 2020.

[24] M. Drela. Xfoil - an analysis and design system for low reynolds number airfoils. in: T.J. Mueller (Ed.) Low Reynolds Number Aerodynamics, Springer-Verlag. Berlin, pages 1–12, 1989.

[25] Ansys fluent user's guide. 2019R1.

[26] Su2 multiphysics simulation and design software. User Guide.

[27] Xia T., Dong H., Yang L., Liu Schicheng, and Jin Z. Investigation on flow structure and aerodynamc characteristics over an airfoil at low reynolds number-a review. AIP Advances 11, 050701, 2021.

[28] J. McAurthur. Aerodynamics of wing at low reynolds numbers: Boundary layer separation and reattachment. Doctor of Philosophy Dissertation, Dept. of Aerospace and Mechanical Engineering, Univ. of Southern California, Los Angeles, CA,, 2008.

[29] McGhee R. J., Walker B. S., and B. F. Millard. Experimental results for the eppler 387 airfoil at low reynolds numbers in the langley low-turbulence pressure tunnel. NASA Technical Memorandum 4062, 1988.

[30] R. B. Langtry and Menter F. R. Correlation-based transition modelling for unstructured parallelized computational fluid dynamics codes. AIAA Journal, 47(12):2894–2906, 2009.

[31] A. Rausa, A. Guardone, and A. Autieri. Implementation of γ-re$_\theta$ transition model with su2: model validation and verification. AIAA Scitech 2023 Forum.